

Nd:YAG laser Thomson scattering diagnostics for a laboratory magnetosphere

| | |
|-------|--|
| メタデータ | 言語: eng 出版者: 公開日: 2021-12-20 キーワード (Ja): キーワード (En): 作成者: Kenmochi, Naoki, NISHIURA, Masaki, yoshida, Zensho, YAMADA, Ichihiro, FUNABA, Hisamichi, SUGATA, T., Nakamura, K., Katsura, S. メールアドレス: 所属: |
| URL | http://hdl.handle.net/10655/00012781 |

This work is licensed under a Creative Commons Attribution 3.0 International License.



Nd:YAG laser Thomson scattering diagnostics for a laboratory magnetosphere

Cite as: Rev. Sci. Instrum. **89**, 10C101 (2018); <https://doi.org/10.1063/1.5037473>

Submitted: 24 April 2018 • Accepted: 18 May 2018 • Published Online: 06 July 2018

 N. Kenmochi,  M. Nishiura, Z. Yoshida, et al.

COLLECTIONS

Paper published as part of the special topic on [Proceedings of the 22nd Topical Conference on High-Temperature Plasma Diagnostics](#)



View Online



Export Citation



CrossMark

ARTICLES YOU MAY BE INTERESTED IN

[Coherence-imaging spectroscopy for 2D distribution of ion temperature and flow velocity in a laboratory magnetosphere](#)

Review of Scientific Instruments **89**, 10D133 (2018); <https://doi.org/10.1063/1.5037124>

[Development of a laser amplification system for the multi-pass Thomson scattering system for GAMMA 10/PDX](#)

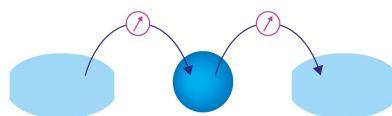
Review of Scientific Instruments **89**, 10C102 (2018); <https://doi.org/10.1063/1.5032224>

[Electro-optic probe measurements of electric fields in plasmas](#)

Review of Scientific Instruments **88**, 023501 (2017); <https://doi.org/10.1063/1.4974740>

Webinar

Interfaces: how they make
or break a nanodevice



March 29th – Register now



Zurich
Instruments



Nd:YAG laser Thomson scattering diagnostics for a laboratory magnetosphere

N. Kenmochi,^{1,a)} M. Nishiura,¹ Z. Yoshida,¹ I. Yamada,² H. Funaba,² T. Sugata,¹ K. Nakamura,¹ and S. Katsura¹

¹Graduate School of Frontier Sciences, The University of Tokyo, 5-1-5 Kashiwanoha, Kashiwa, Chiba 277-8561, Japan

²National Institute for Fusion Science, 322-6 Oroshi-cho, Toki, Gifu 509-5292, Japan

(Presented 18 April 2018; received 24 April 2018; accepted 18 May 2018; published online 6 July 2018)

A new Nd:YAG laser Thomson scattering (TS) system has been developed to explore the mechanism of high-beta plasma formation in the RT-1 device. The TS system is designed to measure electron temperatures (T_e) from 10 eV to 50 keV and electron densities (n_e) of more than $1.0 \times 10^{17} \text{ m}^{-3}$. To measure at the low-density limit, the receiving optics views the long scattering length (60 mm) using a bright optical system with both a large collection window (260-mm diameter) and large collection lenses (300-mm diameter, a solid angle of $\sim 68 \times 10^{-3} \text{ str}$). The scattered light of the 1.2-J Nd:YAG laser (repetition frequency: 10 Hz) is detected with a scattering angle of 90° and is transferred via a set of lenses and an optical fiber bundle to a polychromator. After Raman scattering measurement for the optical alignment and an absolute calibration, we successfully measured $T_e = 72.2 \text{ eV}$ and $n_e = 0.43 \times 10^{16} \text{ m}^{-3}$ for the coil-supported case and $T_e = 79.2 \text{ eV}$ and $n_e = 1.28 \times 10^{16} \text{ m}^{-3}$ for the coil-levitated case near the inner edge in the magnetospheric plasmas. *Published by AIP Publishing.*
<https://doi.org/10.1063/1.5037473>

I. INTRODUCTION

The Ring Trap 1 (RT-1) device creates a laboratory magnetosphere that is obtained via a levitated superconducting ring magnet in a vacuum.¹ The RT-1 experiment forms a peaked density profile, which is spontaneously created via “inward diffusion.”^{2,3} Stable confinement of high-beta plasmas (local electron beta ~ 1) has also been reported in RT-1 magnetospheric plasmas.³ The coexistence of electrons with heterogeneous energies (low energy $\sim 60 \text{ eV}$ and high energy $\sim 50 \text{ keV}$) has recently been found via spectroscopic measurements of the helium-line ratio and X-ray measurements in the RT-1. In addition, high-energy electrons are trapped in the outer confinement region. This result infers a spatial structure similar to the Van Allen belts in the Earth’s magnetosphere. For the density profile, we developed a density reconstruction method from the interferometer data^{2,4} and modified it by introducing a new model function and a global optimization fit to obtain a realistic profile.⁴ Even though helium-line ratio-spectroscopy provides the electron density and the temperature for the low-energy component, an accurate profile of the neutral density is necessary to estimate the local quantities. A Thomson scattering (TS) diagnostic is one method to obtain them.^{5,6} Therefore, we have started the development of a TS diagnostic system for the RT-1.

This article describes the development of the TS diagnostic system for the RT-1. The specifications required to satisfy the TS diagnostic are severe because the electron density (n_e) is close to the lower detection limit of $n_e \sim 10^{17} \text{ m}^{-3}$ or less. Comments concerning the absolute calibration for the density measurement are included in the text. The initial results of the TS measurement for the RT-1 plasma are shown at the end of the article.

II. DESCRIPTION OF THE SYSTEM

A. Laser system

Figure 1 shows a bird’s eye view of the TS system on the RT-1 device (the upper vacuum vessel is open for a cut view). The TS system consists of a Nd:YAG laser, a beam dump, collection optics, and an interference polychromator. The laser beams are introduced into the plasma through a horizontal port, which passes through the RT-1 device at $r = 0.45 \text{ m}$. The scattered light with an angle of 90° is collected by a set of collection lenses with a solid angle of $68 \times 10^{-3} \text{ str}$ into the entrance of a fiber bundle, which guides the light to a polychromator. The designed target plasma range is $10 \text{ eV} < T_e < 50 \text{ keV}$ and $n_e > 0.5 \times 10^{17} \text{ m}^{-3}$.

A Nd:YAG laser produces high-power Q-switched pulses. Table I summarizes the specifications of the Nd:YAG laser. The injection optics transfers the laser light into the vacuum vessel of the RT-1 through a quartz window that has anti-reflection coating. The laser head is mounted on a table fixed on the floor of the RT-1 hall. The distance between the exit aperture of the laser head and the vacuum boundary of the RT-1 port

Note: Paper published as part of the Proceedings of the 22nd Topical Conference on High-Temperature Plasma Diagnostics, San Diego, California, April 2018.

^{a)}Author to whom correspondence should be addressed: kenmochi@edu.k.u-tokyo.ac.jp

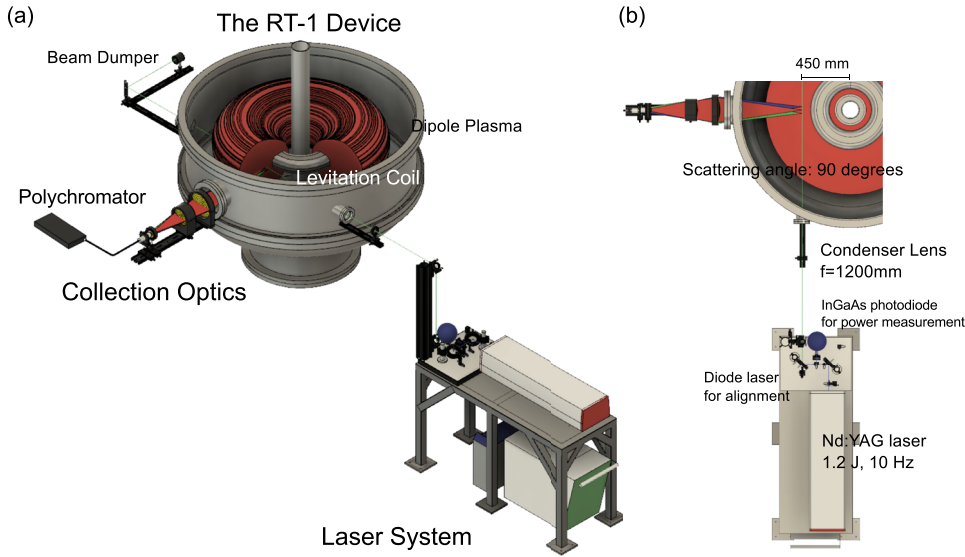


FIG. 1. (a) Overview and (b) sideview of the TS system in the RT-1 device.

TABLE I. Specifications of the Nd:YAG laser.

| Parameter | Specification |
|----------------------|---------------|
| Energy (J) | 1.2 |
| Repetition rate (Hz) | 10 |
| Pulse width (ns) | 5–8 |
| Beam diameter (mm) | 7 |
| Energy stability (%) | 2 |

is ~ 4 m. The laser optics consists of four relay mirrors and a biconvex lens (BK7, $\Phi 30$, $f = 1200$ mm) for focusing. To improve the signal-to-noise ratio, the laser beam is focused on the diagnosing point with a design diameter of $80 \mu\text{m}$. The Nd:YAG laser beam is collinearly aligned using a diode laser beam at a wavelength of 640 nm as a visible guide line. The laser beam is reflected by 90° at the opposite side of the injection port and is introduced into the beam dump. To measure power, an InGaAs photodiode detects the scattering light of the laser near the injection mirror.

B. Collection optics

The collection optics consists of six lenses, which connect image light to an optical fiber bundle. Figure 2 shows a schematic of the collection optics. The specifications are detailed in Table II. The observation optics was optimized using the optical engineering program ZEMAX to suppress the monochromatic and color aberrations and to minimize the transmission losses of the collected light from 700 nm to

TABLE II. Specification of the collection optics.

| Parameter | Specification |
|---------------------------------|--------------------------|
| Wavelength (nm) | 700–1064 |
| Scattering length (mm) | 60 |
| Solid angle (str) | $\sim 68 \times 10^{-3}$ |
| Magnification | 0.5 |
| NA (scattered point) | 0.145 |
| NA (collection point) | 0.28 |
| Length between object and image | 1430.6 |
| Transmission (700–1064 nm) (%) | ~ 80 |
| Imaging area (mm) | $\Phi 70$ |
| Material | BK7, SF6 |

1064 nm . The collection optics is designed to detect the scattered light in the sample volume with a scattering length of 60 mm , where $z = 0 \text{ m}$ and $r = 0.45 \text{ m}$. At this location, the diameter of the laser beam is focused within less than 0.1 mm at a solid angle of $\sim 68 \times 10^{-3} \text{ str}$ (with a scattering angle of 90°). The long scattering length and the large solid angle make it possible to detect a sufficient number of photons ($> 10^4$ photons) for low-density ($n_e \sim 10^{17} \text{ m}^{-3}$) plasmas. The collected light is focused on a fiber bundle with a magnification of 0.5 (see Fig. 3). The receiving area of the optical fiber bundle with 31 fibers is $30.4 \text{ mm} \times 0.98 \text{ mm}$. The core and cladding diameters are 0.79 mm and 0.98 mm , respectively. The exit of the optical fiber bundle is converted to match the circular-shaped bundle. The scattered light is guided to a polychromator via the optical fiber bundle.

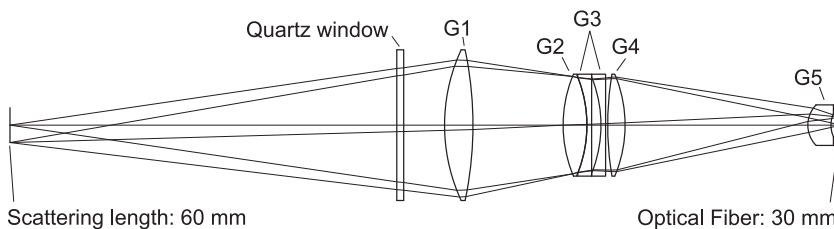


FIG. 2. The set of collection optics lenses. The G1, G2, G4, and G5 lenses are convex, and the two G3 lenses are concave.

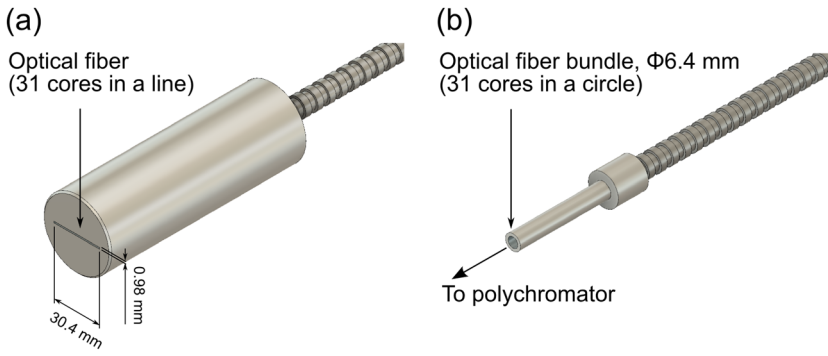


FIG. 3. Schematic of the optical fiber bundle: (a) the optical fiber on the input side of the scattered light and (b) the optical fiber bundle on the output side, which is inserted into the polychromator.

C. Polychromator and data acquisition

The scattered light is analyzed by an interference-type polychromator. The polychromator has the same specifications as that used in Heliotron J⁷⁻⁹ and consists of interference filters, relay lenses, avalanche photodiodes (APDs; Hamamatsu photonics K.K., S 8890-30), and fast-response preamplifiers. The scattered light is cascaded to five interference filters using relay lenses and is divided into five spectral channels. The separated light is then focused onto each APD detector. The spectral sensitivities of the polychromator filters are obtained via a calibration light source. The result is plotted as a function of the wavelength in Fig. 4. The five channels cover the detection of the scattered light at an electron temperature of 50 keV in the RT-1 device. The detected signals are fed into a four-channel high-speed oscilloscope (Tektronix, DPO4054B) with a bandwidth of 500 MHz and a sampling rate of 2.5 GS/s. The data are transferred to a PC for analysis.

III. ALIGNMENT AND OVERALL DETECTION EFFICIENCY BY RAMAN SCATTERING

To adjust the optical alignment and calibrate the overall sensitivities detected at the polychromator for an absolute n_e measurement, a Raman scattering experiment of nitrogen molecules (N_2) was conducted. Figure 5 shows the

dependence of the scattered signal on the N_2 gas pressure. Because the measured signal is proportional to the N_2 gas density, the overall detection efficiency $\gamma = V/n_e$ is calculated using the known cross section for Raman scattering.¹⁰ This procedure converts the measured TS signals for each channel to n_e (see Fig. 6). The result indicates that the TS system detects TS signals at several tens of mV, which is a sufficiently larger value than the noise level, several mV, even though it was a low-density plasma ($n_e \sim 10^{17} \text{ m}^{-3}$).

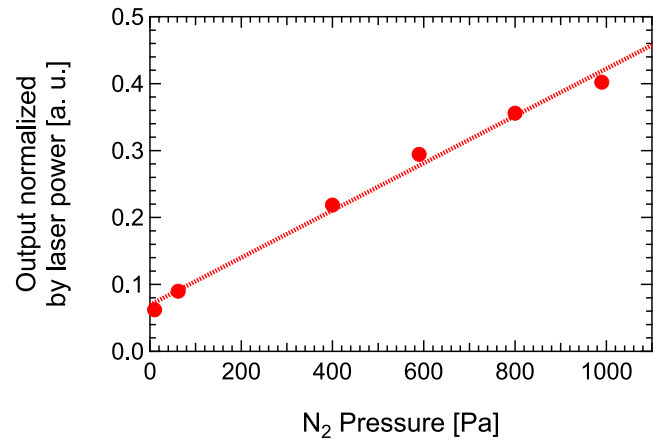


FIG. 5. Dependence of the Raman scattering signal on the N_2 gas pressure.

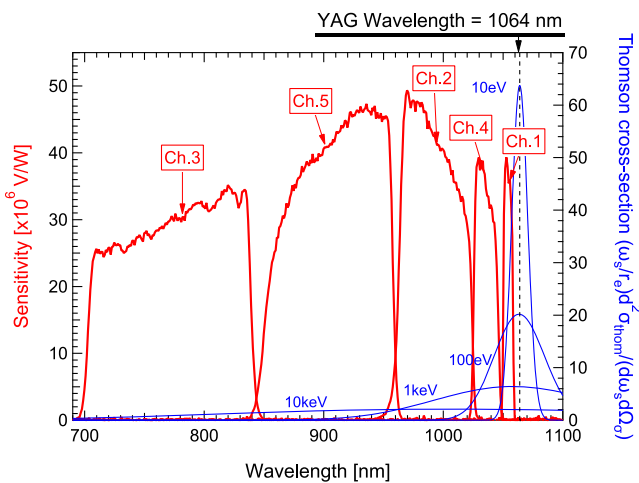


FIG. 4. Spectral sensitivity of the polychromator filters (red) and the spectra of the Thomson cross section (blue).

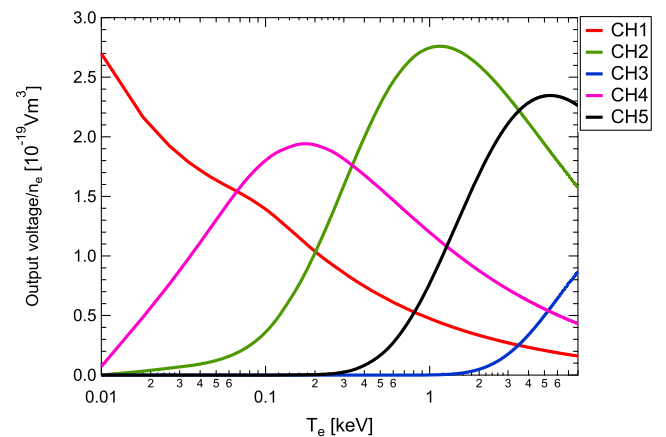


FIG. 6. Calibration factor for the density measurement of each wavelength channel of the polychromator.

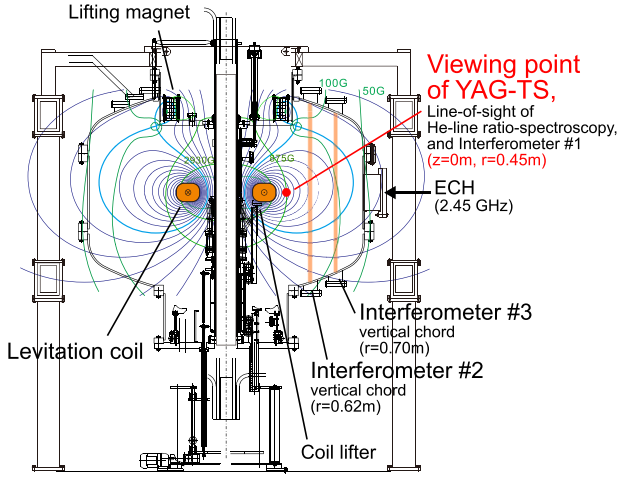


FIG. 7. Cross-sectional view of the RT-1 magnetospheric plasma device.

IV. INITIAL RESULTS

Figure 7 shows the cross section of the RT-1 device with the measurement instruments. The magnetic field lines are superimposed on the cross section. For the plasma experiments, the superconducting magnet inside the vacuum vessel operated in two operational modes: in one, the levitation coil was supported by the coil lifter (the coil-supported case) and, in the other, the levitation coil was levitated by the lifting magnet (the coil-levitated case). The plasma in this experiment was produced via electron cyclotron heating at 17 kW with helium gas at pressures of 6 mPa and 0.7 mPa in the coil-supported and coil-levitated cases, respectively. Figure 8 shows the time evolution of the line-integrated electron density $n_e L$ and the diamagnetism in the two cases. Interferometer (IF) #1 measures the density on the horizontal chord passing through $r = 0.45$ m. IFs #2 and #3 measure the densities on vertical

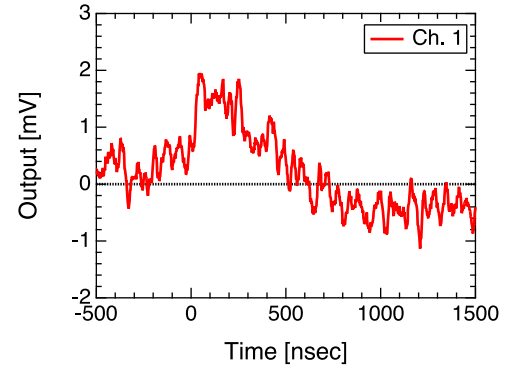


FIG. 9. The output signal of the polychromator (Ch. 1) in the coil-levitated case. The background level has been removed.

chords through $r = 0.62$ and 0.7 m, respectively. In the coil-levitated case, the electron pressure is much higher than that in the coil-supported case. This is explained by the production of high-energy electrons of a few tens of keV, which increases the temperature rather than the density. However, the density of high-energy electrons is localized and is too low to be detected by the TS diagnostic. In these experiments, we averaged the scattered light for eight shots between $t = 1.1$ s and 1.9 s. Figure 9 shows the output signal of the polychromator (Ch. 1) whose bandwidth ranged from 1050 nm to 1055 nm in the coil-levitated case. The background level before shooting the laser was subtracted from the measured data. The repeatable stray light that is mainly caused by the reflection from the surface of the levitation coil was measured without the discharge and was subtracted from the signal. The signal was accumulated in a series of 30 reproducible discharges of the RT-1 device to subtract the stray light precisely. Three channels (Ch. 1, 2, and 4) were used to calculate T_e and n_e . The measurement results of the TS diagnostic are summarized in Table III in conjunction with the data from the helium-line ratio-spectroscopy and the interferometers. Because of the low electron densities, the error bars of the TS diagnostic for the temperature, which show the standard errors for the spectral fitting, are large in these experimental conditions. As indicated in Fig. 7, the TS system measures the local point ($r = 0.45$ m and $z = 0$ m). Helium-line ratio-spectroscopy measures the line-integrated T_e and n_e (through $r = 0.45$ m and $z = 0$ m) from the intensity ratio of the neutral-helium lines: 388 nm, 447 nm, 706 nm, and 728 nm. The line-integrated T_e and n_e are calculated via the intensity ratio of the 728 nm–706 nm lines and the 447 nm–388 nm lines, respectively. Despite the direct comparison between the local and integrated quantities, the n_e and T_e values measured by the TS system and the helium-line ratio-spectroscopy tend to increase in the coil-levitated case.

A method to reconstruct the density from IFs #1, #2, and #3 was developed in Ref. 2 and modified in Ref. 4. Note that the sample point of the TS diagnostic exists in the inner edge of the peaked n_e profile. n_e in this area steeply decreases to zero toward the levitated coil. Even though n_e for the TS diagnostic is lower than the reconstructed n_e at the same point by a factor of 0.12, we believe that the measured results are appropriate quantities. The result indicates that the TS diagnostic is able to measure T_e and n_e even in the low-density limit ($n_e \sim 0.5 \times 10^{16} \text{ m}^{-3}$).

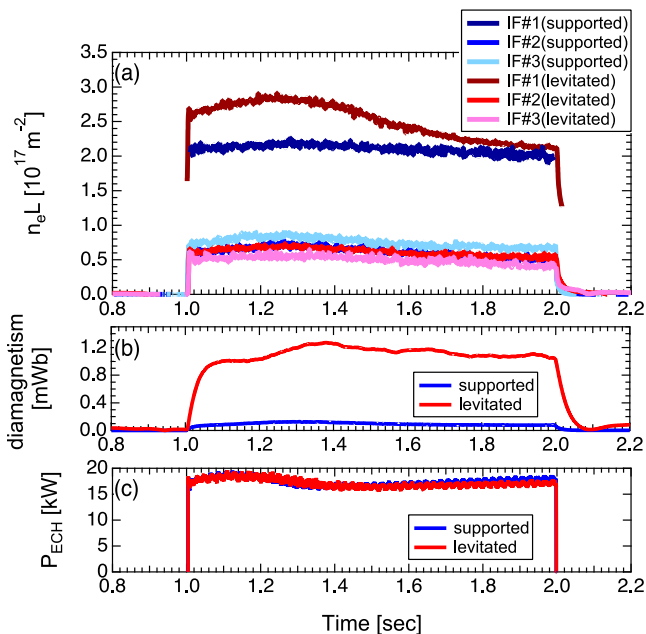


FIG. 8. Time evolution of (a) the line-integrated electron density, (b) the diamagnetism, and (c) the injection power of ECH in the coil-supported and coil-levitated cases.

TABLE III. Plasma parameters obtained by the TS diagnostic (boldface values) and other diagnostics in the coil-supported and coil-levitated cases.

| | Diamagnetism (mWb) | Electron density | | | | | Electron temperature | |
|----------------|-----------------------|---|---|---|---|--|-----------------------------------|--|
| | | n_e (Thomson) (10^{16} m^{-3}) | $n_e L$ (IF #1) (10^{16} m^{-2}) | $n_e L$ (IF #2) (10^{16} m^{-2}) | $n_e L$ (IF #3) (10^{16} m^{-2}) | n_e (line ratio of neutral He) (10^{16} m^{-3}) | T_e (Thomson) (eV) | T_e (line ratio of neutral He) (eV) |
| Coil supported | 0.106 | 0.43 ± 0.05 | ... | 5.68 | 6.86 | 5.66 | 72.2 ± 31.9 | 20.5 |
| Coil levitated | 1.275 | 1.28 ± 0.22 | 25.3 | 5.53 | 4.62 | 7.89 | 79.2 ± 46.0 | 21.7 |

V. SUMMARY

A TS system was developed to measure the electron temperature and density in the RT-1 device. The TS system comprises a Nd:YAG pulse laser, a beam dump, the collection lens optics, and a polychromator. For an electron density of more than 10^{17} m^{-3} , we designed the collection optics with a scattering length of 60 mm and a large solid angle of $\sim 68 \times 10^{-3} \text{ str}$ to increase the photon number. After the alignment and efficiency test of the TS system via a Raman scattering experiment, we successfully measured $T_e = 79.2 \text{ eV}$ at $n_e = 1.28 \times 10^{16} \text{ m}^{-3}$ close to the lower measurement limit of the electron density. These experimental results are a first step toward profile measurement in the high-beta plasmas of the RT-1 device.

ACKNOWLEDGMENTS

This work is supported by the NIFS Collaboration Research Program (No. NIFS15KOA034) and JSPS KAKENHI Grant Nos. 17H01177 and 18K13525. One of the authors (M.N.) would like to thank Associate Professor A. Ejiri of The University of Tokyo for his advice.

- ¹Z. Yoshida, H. Saitoh, J. Morikawa, Y. Yano, S. Watanabe, and Y. Ogawa, *Phys. Rev. Lett.* **104**, 235004 (2010).
- ²H. Saitoh, Y. Yano, Z. Yoshida, M. Nishiura, J. Morikawa, Y. Kawazura, T. Nogami, and M. Yamasaki, *Phys. Plasmas* **21**, 082511 (2014).
- ³M. Nishiura, Z. Yoshida, H. Saitoh, Y. Yano, Y. Kawazura, T. Nogami, M. Yamasaki, T. Mushiaki, and A. Kashyap, *Nucl. Fusion* **55**, 053019 (2015).
- ⁴M. Nishiura, Y. Kawazura, Z. Yoshida, N. Kenmochi, Y. Yano, H. Saitoh, M. Yamasaki, T. Mushiaki, A. Kashyap, N. Takahashi, M. Nakatsuka, and A. Fukuyama, *Nucl. Fusion* **57**, 086038 (2017).
- ⁵H. Murmann, S. Götsch, H. Röhr, H. Salzmann, and K. H. Steuer, *Rev. Sci. Instrum.* **63**, 4941 (1992).
- ⁶T. N. Carlstrom, G. L. Campbell, J. C. DeBoo, R. Evanko, J. Evans, C. M. Greenfield, J. Haskovec, C. L. Hsieh, E. McKee, R. T. Snider, R. Stockdale, P. K. Trost, and M. P. Thomas, *Rev. Sci. Instrum.* **63**, 4901 (1992).
- ⁷T. Minami, S. Kobayashi, T. Mizuuchi, H. Yashiro, M. Takeuchi, S. Ohshima, S. Yamamoto, H. Okada, K. Nagasaki, Y. Nakamura, K. Hanatani, S. Konoshima, and F. Sano, *Rev. Sci. Instrum.* **81**, 10D532 (2010).
- ⁸T. Minami, S. Arai, N. Kenmochi, H. Yashiro, C. Takahashi, S. Kobayashi, T. Mizuuchi, S. Ohshima, S. Yamamoto, H. Okada, K. Nagasaki, Y. Nakamura, K. Hanatani, S. Konoshima, and F. Sano, *Plasma Sci. Technol.* **15**(3), 240 (2013).
- ⁹N. Kenmochi, T. Minami, C. Takahashi, S. Tei, T. Mizuuchi, S. Kobayashi, K. Nagasaki, Y. Nakamura, H. Okada, S. Kado, S. Yamamoto, S. Ohshima, S. Konoshima, N. Shi, L. Zang, Y. Ohtani, K. Kasajima, and F. Sano, *Rev. Sci. Instrum.* **85**, 11D819 (2014).
- ¹⁰J. Howard, B. W. James, and W. T. B. Smith, *J. Phys. D: Appl. Phys.* **12**, 1435 (1979).